Braeuer, B., Asch, G., Hofstetter, R., Haberland, C., Jaser, D., El-Kelani, R., Weber, M. (2012): Microseimicity distribution in the southern Dead Sea area and its implications on the structure of the basin. - Geophysical Journal International, 188, 3, pp. 873—878.

DOI: http://doi.org/10.1111/j.1365-246X.2011.05318.x

Geophysical Journal International

Geophys. J. Int. (2012) **188,** 873–878 doi: 10.1111/j.1365-246X.2011.05318.x

Microseismicity distribution in the southern Dead Sea basin and its implications on the structure of the basin

B. Braeuer,[1] Guenter Asch,[1] R. Hofstetter,[2,★] Ch. Haberland,[1] D. Jaser,[3] R. El-Kelani[4] and M. Weber[1,5]

[1] *GFZ German Research Centre for Geosciences, Telegrafenberg,* 14473 *Potsdam, Germany. E-mail: ben@gfz-potsdam.de*
[2] *Geophysical Institute of Israel (GII),* P.O. Box 182, *Lod* 71100, *Israel*
[3] *Natural Resources Authority (NRA), Eight circle,* P.O. Box 7, *Amman, Jordan*
[4] *An-Najah National University,* P.O. Box 7, *Nablus, West Bank, Palestine*
[5] *Institute of Earth and Environmental Science, Karl-Liebknecht-Str.* 24-25, 14476 *Potsdam, University of Potsdam, Germany*

Accepted 2011 November 27. Received 2011 October 14; in original form 2011 August 8

SUMMARY

While the Dead Sea basin has been studied for a long time, the available knowledge about the detailed seismicity distribution in the area, as well as the deeper structure of the basin, is limited. Therefore, within the framework of the international project DESIRE (DEad Sea Integrated REsearch project), a dense temporary local seismological network was operated in the southern Dead Sea area. We use 530 local earthquakes, having all together 26 730 *P*- and *S*-arrival times for a simultaneous inversion of 1-D velocity models, station corrections and precise earthquake locations. Jackknife tests suggest an accuracy of the derived hypocentre locations of about 1 km. Thus, the result is the first clear image of the absolute distribution of the microseismicity of the area, especially in depth. The seismicity is concentrated in the upper crust down to 20 km depth while the lower limit of the seismicity is reached at 31 km depth. The seismic events at the eastern boundary fault (EBF) in the southern part of the study area represent the northward transform motion of the Arabian Plate along the Dead Sea Transform. North of the Boqeq fault the seismic activity represents the transfer of the motion in the pull-apart basin from the eastern to the western boundary. We find that from the surface downward the seismic events are tracing the boundary faults of the basin. The western boundary is mapped down to 12 km depth while the EBF reaches about 17 km depth, forming an asymmetric basin. One fifth of the data set is related to a specific cluster in time and space, which occurred in 2007 February at the western border fault. This cluster is aligned vertically, that is, it is perpendicular to the direction of the dominating left-lateral strike-slip movement at the main transform fault.

Key words: Seismicity and tectonics; Continental tectonics: strike-slip and transform; Asia.

1 INTRODUCTION

The Dead Sea transform (DST) fault is one of the largest transform faults in the world with a length of about 1000 km. It forms the boundary between the Arabian Plate and the African Plate (Fig. 1). The relative left-lateral motion of these two plates, which started in the early Miocene (∼20 Ma), caused a total shift of ∼107 km (Quennel 1958; Freund *et al.* 1970). This relative motion resulted in creating the Dead Sea Basin (DSB), one of the largest pull-apart basins in the world. Two main properties make it a unique place to study: (1) its special geometry, very deep [depth: 11–16 km for the southern part (ten Brink *et al.* 1993; Ginzburg & Ben-Avraham 1997; Mechie *et al.* 2009)] and narrow (∼16 km wide) relative to its length (107–230 km) depending on the definition of its northern and southern boundaries (ten Brink *et al.* 1993; Larsen *et al.* 2002; Ben-Avraham & Lazar 2006; Shamir 2006); (2) the two strike-slip faults bordering the basin to the East (Arava Fault) and to the West (Jericho Fault), which have moved approximately parallel to each other during the complete formation of the basin. Therefore, it is considered a prime location to study pull-apart basins. Despite the large amount of studies that were made in the Dead Sea region, little is known about the deeper structure of the DSB and therefore the distribution of the local seismicity is used in this study to shed light on it. A distinct picture of the seismic activity at the different faults is a subject of this study.

Thick layers of sediments fill the basin (Zak & Freund 1981). Clastics and evaporites were deposited during periods of different climate and varying water sources (fresh or salt), which transported the sediments into the basin (Garfunkel & Ben-Avraham 1996). Some of the evaporites ascended at fault zones and formed two

★Correction made after online publication 2012 January 19: this author's surname has been corrected.

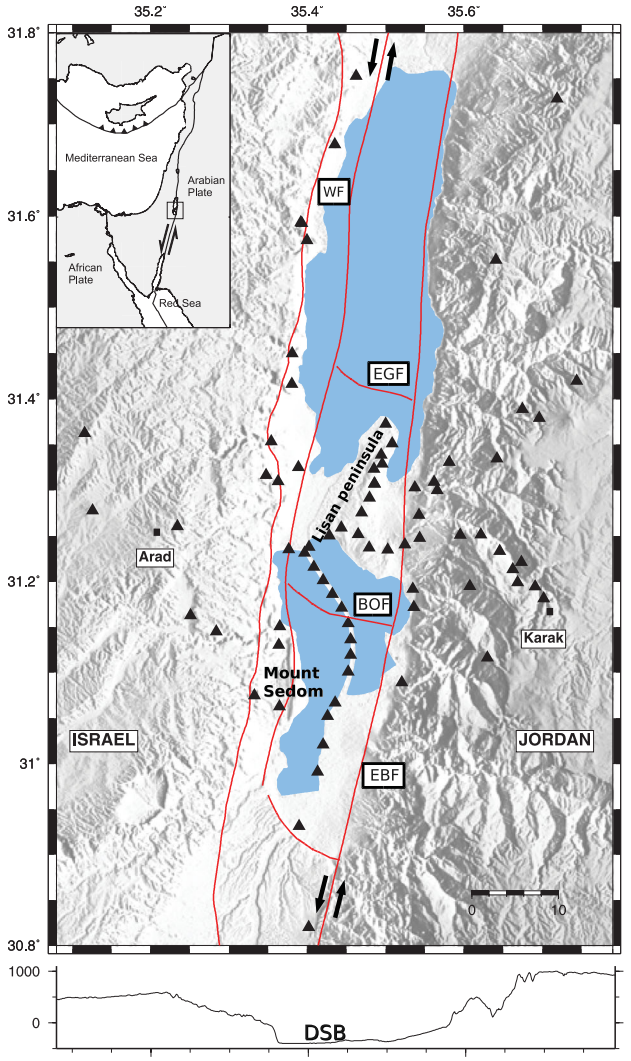

Figure 1. (Top) Station distribution (triangles) and tectonic setting in the southern DSB simplified after Garfunkel (1997), Larsen *et al.* (2002) and Smit *et al.* (2008). The areas which are covered with water recently are marked in blue. Used stations from the permanent networks in Israel and Jordan are also marked. Only the main faults are indicated as solid red lines. Eastern border fault (EBF), Jericho fault and Western Boundary fault, here collectively called Western faults (WF). The two faults bordering the Lisan Peninsula: Ein Gedi Fault (EGF) and Boqeq fault (BOF). (Bottom) Topographic profile from West to East at 31.25°N.

prominent salt diapirs within the basin: the Sedom diapir in the southwest of the basin (below Mount Sedom in Fig. 1) and the Lisan diapir, situated in the centre of the basin, dividing it into two parts (Ginzburg & Ben-Avraham 1997). These authors inferred this division from an abrupt change of depth from 6 to 8 km north of the diapir to 14 km below the diapir.

The DSB is bounded to the East by the Arava or eastern boundary fault (EBF in Fig. 1). To the West the basin is bounded by the Jericho Fault (strike-slip) and the Western Boundary fault (normal fault), here collectively called Western faults (WF in Fig. 1). The secondary transverse Ein Gedi fault (EGF in Fig. 1) and Boqeq Fault (BOF in Fig. 1) are bordering the Lisan diapir to the north and the south, respectively (e.g. Ben-Avraham & Ten Brink 1989).

The seismic activity at the DST in general is small compared to other transform faults (Begin & Steinitz 2005). However, these authors showed that the relationship between fault offset and number of earthquakes proposed by Wesnousky (1990) for California, is also valid for the DST. In several studies of the seismicity along the DST (van Eck & Hofstetter 1989, 1990; Aldersons *et al.* 2003; Begin & Steinitz 2005) the DSB is found to be one of the main regions of seismic activity. Using data from stations on both sides of the basin, Aldersons *et al.* (2003) determined the depth of the local events. Unlike other basins (Meissner & Strehlau 1982; Chen & Molnar 1983) and other strike-slip regions (e.g. Thurber *et al.* 2006) they observed that most of the microseismic activity occurred at depth greater than 20 km.

2 EXPERIMENT AND DATA

In 2006 October a seismic array of 65 stations was installed in the southern Dead Sea area along the border region of Israel and Jordan (Fig. 1). The stations were located in the DSB as well as on the shoulders east and west of the main border faults. A total of 38 stations were equipped with Mark L-4C-3D short period sensor, sampled at 200 Hz in high gain mode. The other 27 recorders were equipped with GURALP CMG-40T or CMG-3T or STS-2 seismometers, all sampled at 100 Hz. In 2008 March, after 17 months of operation time, all stations were dismantled. The mean station spacing was about 5 km in Israel and 3 km in Jordan. On average the network recorded one to two local events per day.

3 DATA PROCESSING AND 1-D VELOCITY MODEL

Event detection was done visually by inspecting each half hour of the data. In total more then 700 events were found. Arrival times were manually picked using JSTAR, a software provided by the Geophysical Institute of Israel (GII). Only events with 12 or more onset times were included, containing at least six *S*-wave observations, and a gap (largest azimuth angle with no observation) $<180°$. This reduced the number to 530 well-constrained events consisting of 13 970 *P*- and 12 760 *S*-wave arrival time observations. These observations were used for a simultaneous inversion of accurate hypocentres, 1-D velocity models and station corrections (Kissling *et al.* 1994). The *P*- and *S*-wave velocity models were determined independently using a v_P/v_S ratio of 1.74 as an initial value (based on Wadati diagram analysis). The final 1-D models consist of 10 layers down to a depth of 30 km. A wide range of initial velocity models (indicated in Fig. 2) were used to investigate the quality and the stability of the final *P*- and *S*-wave velocity models. A first-arrival tomography of a controlled source seismic experiment (Paschke *et al.* 2011) crossing the study area from the West to East showed clearly that the uppermost 2 km are laterally very inhomogeneous, for example, the *P*-wave velocity at 1 km depth is varying between 3.5 and 5 km s^{-1}. This explains the varying velocity values (for different start models) for the first layer (Fig. 2). The *P*-wave velocity model in Fig. 2 starts at 3.6 km s^{-1} at the surface and reaches 6.4 km s^{-1} at 30 km depth. Due to the fact that most of the earthquakes occur in the upper 17 km and the seismicity does not occur at depth greater than ∼30 km, between 20 and 30 km depth the resolution is limited. The *S*-wave velocity is very low (1.3 km s^{-1}—lower than all the tested start models) in the uppermost 2 km due to weathered and partly water-saturated rocks near the surface in the basin. Therefore, the v_P/v_S ratio is high, about 2.9. In the next layer the *S*-wave velocity is 2.3 km s^{-1} and at 30 km depth it reaches 3.7 km s^{-1}. The v_P/v_S ratio shows small variations in the subsequent layers having an average value of 1.74.

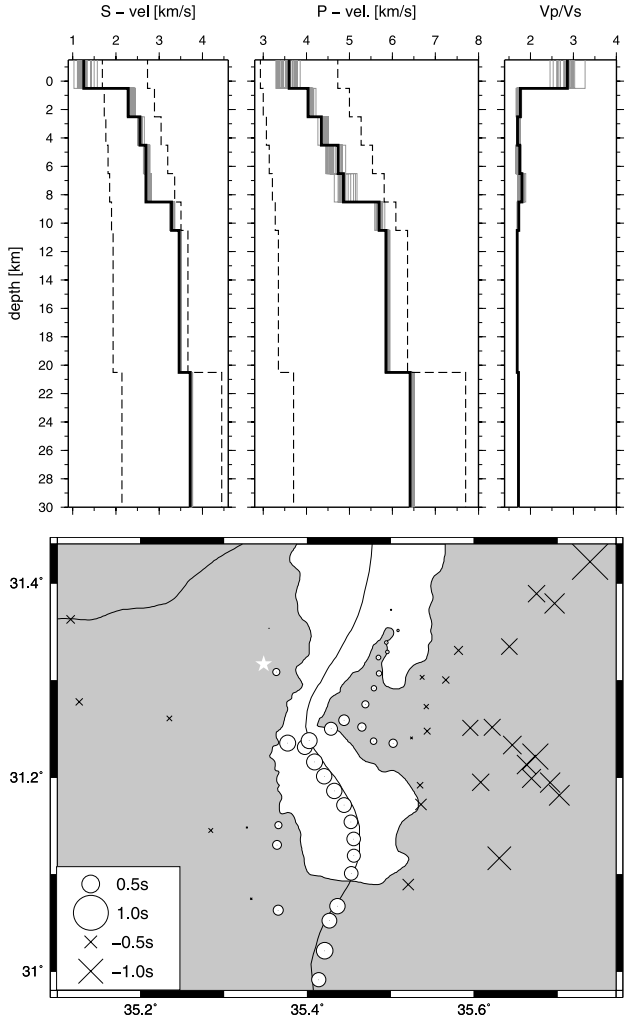

Figure 2. (Top panel) 1-D velocity models for S and P waves and v_P/v_S ratio. All resulting models from 36 different starting models are shown in grey. Solid black lines indicate the best final model with lowest rms. Dashed lines indicate the limits of the used starting models. (Bottom panel) Corresponding P-wave station corrections. The reference station is indicated by a star.

A geological interpretation of the 1-D velocity models, laterally averaging over crystalline basement and a huge sediment basin, is limited. The velocity values for the upper 10 km incorporate upper crustal values [5–6 km s^{-1} after ten Brink *et al.* (2006) and Mechie *et al.* (2009)] and values in the sedimentary basin [3.5–4.5 km s^{-1} after ten Brink *et al.* (2006) and Mechie *et al.* (2009)]. Due to a majority of ray paths crossing the sedimentary basin, the velocities presented here are closer to those of the basin. The layer between 10 and 20 km represents the sedimentary basin [down to 14 km depth following Ginzburg & Ben-Avraham (1997)] and the lower crust (below 14 km depth), also resulting in an average value between upper crust and sediments.

Station corrections are introduced to also find an appropriate 1-D model in laterally heterogeneous areas (Kissling *et al.* 1995). The station corrections (relative to the reference station; Fig. 2 bottom panel) are in the range of -1.45 to $+0.47$ s. In general, one can see larger values of station corrections (related to low velocities) in the basin and smaller values (high velocities) on the shoulders of the basin. Furthermore, the corrections on the eastern shoulder are smaller than on the western shoulder.

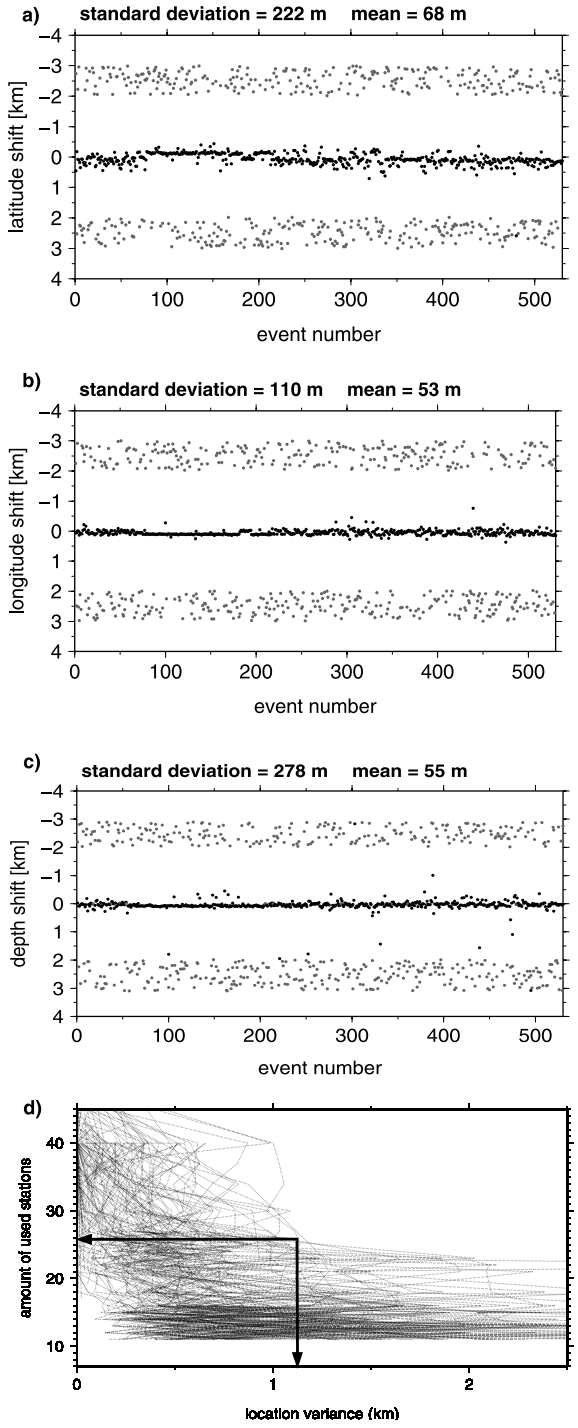

Figure 3. Stability tests: (a) Mislocation of hypocentres that are randomly shifted by 2-3 km in direction north–south, (b) east–west and (c) in the depth, before being introduced into the 1-D velocity inversion. Grey dots denote the shifted hypocentral locations and black dots denote the relocalized hypocentres after the shifting. (d) Subsets of observations for certain events randomly selected and relocated to estimate location accuracy (jackknife test). Location variance is plotted against the number of stations used. The arrows are indicating the location variance (about 1 km) for the average number of stations (26), which is assumed to be representative for the average hypocentre accuracy.

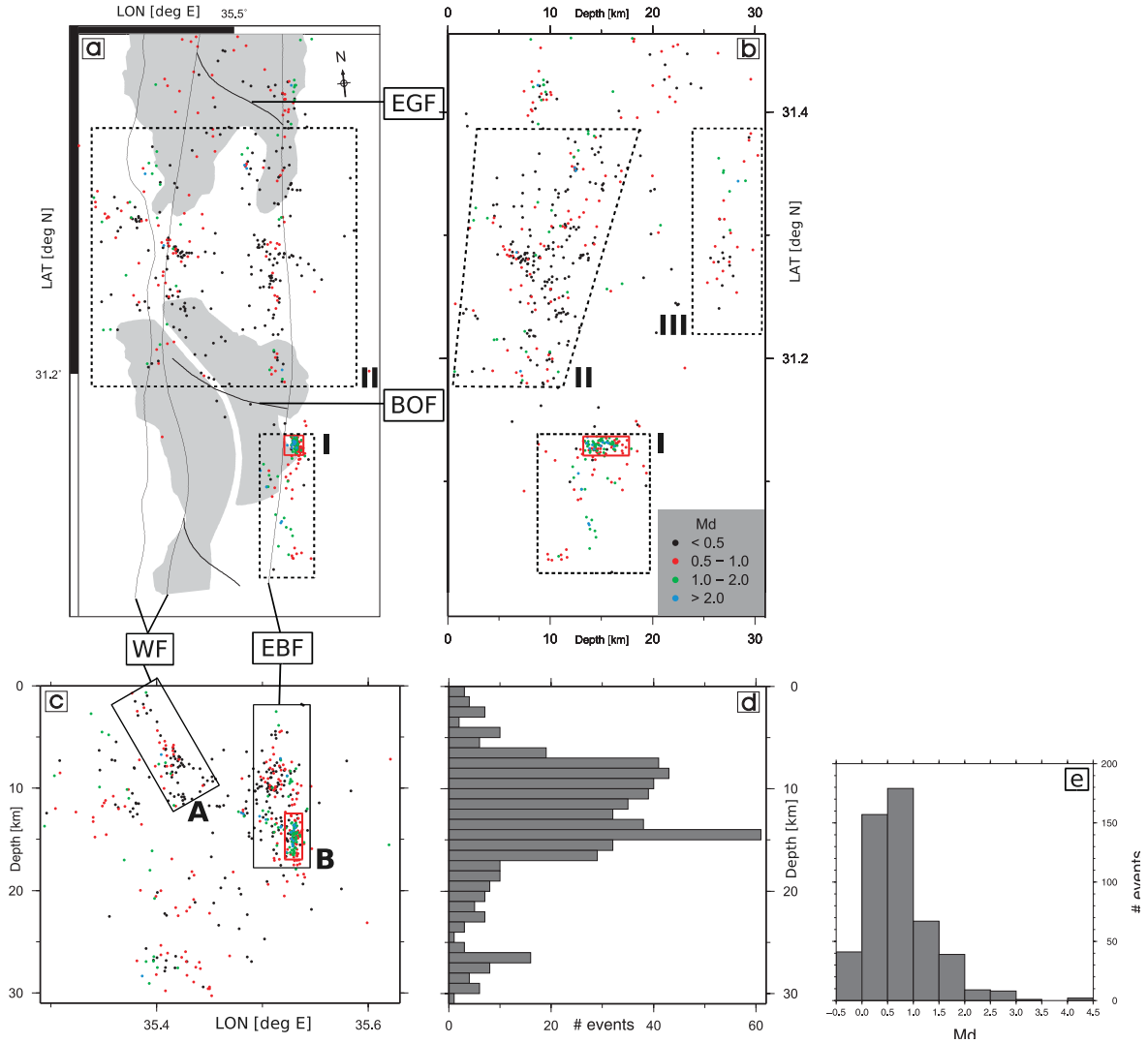

Figure 4. (a) Map of the study area, rotated 8° ccw to align approximately with the direction of the main border faults; (b) projected hypocentres on a vertical cross-section along the main axis of the DSB; (c) projected hypocentres on a vertical cross-section along the transverse axis of the DSB and (d) histogram of events per depth kilometre. The boxes assign areas discussed in detail in the text. (e) Number of events per magnitude step of 0.5. The derived magnitude of completeness is $M_c = 0.5$.

To assess the quality and stability of the 1-D model several tests were carried out. Shifting the initial values of the hypocentral coordinates randomly by a few kilometres and then introducing them into the joint velocity hypocentre inversion, provides a check for a potential bias in the hypocentre locations and for the stability of the solution to the coupled problem (Figs 3a–c, Husen *et al.* 1999). If the proposed 1-D velocity model indicates a robust minimum in the solution space, no significant changes in velocity and hypocentre locations are expected. The location errors yield a standard derivation of 100–200 m for the horizontal coordinates and about 300 m for the depth. With these small values it is reasonable to assume that the inverted velocity model is the global minimum of the inversion.

The accuracy of the obtained hypocentres can be verified with a jackknife test (Fig. 3d; Lange 2008), that is, subsets of observations for certain events are selected randomly and relocated with the final velocity model. For relocations with 26 stations, which is the average amount of stations for all events, we obtain a variance of about 1 km (Fig. 3). This is assumed to be representative for the hypocentre accuracy and is confirmed by a similarly small misfit of the relocalization of an artificial explosion in the area.

For the magnitude determination, the duration magnitude scale M_d (magnitude employing the fact that the total length of the seismic wave train reflects the size of the event, Solov'yev 1965) used by the GII for the region was applied. The magnitude of completeness (M_c: lowest magnitude at which 100 per cent of the events in a space–time volume are detected, Rydelek & Sacks 1989) is about 0.5 (Fig. 4e), which shows the uniqueness of the data set for the region as none of the older data sets had an M_c lower than 2.

4 RESULTS AND DISCUSSION

Seismicity occurs close to the surface and down to depths of 31 km, which agrees with Aldersons *et al.* (2003). Fig. 4 shows the first accurate image of the distribution of microearthquakes in the southern DSB. In the south of the investigation area (south of 31.13°N, I in Fig. 4) the seismic activity is solely related to the EBF. These events occur mainly between 12 and 17 km depth. From 2007 February 9 to

2007 February 27 spatial and temporal clustering of 110 events also occurred here (red box in Fig. 4a–c). The first and the third events of this cluster were the largest of all events during the recording period (M_d 3.5 and 4.5, respectively). The cluster is located on the EBF, and surprisingly it extends vertically and not horizontally in the direction of the main left lateral strike-slip movement (compare the red boxes in Figs 4b and c and in Fig. 4a). North of the cluster a seismically inactive region extends to 31.17°N where shallow activity (1–12 km depth) starts on both boundaries (II in Fig. 4). This change in the seismic behaviour can be associated with the transverse BOF (BOF in Fig. 4). The lower boundary of the seismic activity in the upper crust [above 20 km depth after Mechie *et al.* (2009)] deepens between BOF and the EGF from 12 to 17 km depth (Fig. 4). It is important to note that this pattern of the seismicity distribution between BOF and EGF is similar for both boundaries (EBF, WF). A similar seismicity distribution pattern was found by van Eck & Hofstetter (1989) for a 20 month period of investigation between 1986 and 1988: Strong activity around 31.12°N only at the EBF, including a cluster, a gap of seismicity farther north, and activity on both boundary faults north of 31.16°N. Thus, this pattern can be assumed to be constant over a longer period.

In the W–E cross-section the seismic events trace the EBF nearly vertically from depth of 2 to 18 km (B in Fig. 4c). The seismic activity along the western boundary (A in Fig. 4c) has a dip of about 60° and is only traceable down to 12 km depth.

In the lower crust (III in Fig. 4b) the distribution of the events appears rather diffuse so the events seem not to be related to fault system of the sedimentary basin. This is consistent with the assumption of Mechie *et al.* (2009) that the boundary between the upper and the lower crust at 20 km depth act as a decoupling zone. While activity at this depth is known also from Aldersons *et al.* (2003), the limited activity does not allow further interpretations.

Due to their small size most of the events are normally not recorded by the permanent networks in Israel and Jordan, which have large spacings between adjacent stations. This explains the large difference between our observations of depth range with highest seismic activity (6–17 km, Fig. 4d) and the observations of Aldersons *et al.* (2003) with highest seismic activity in a depth range of 15–30 km.

5 CONCLUSIONS

The unusually deep limit of seismicity for such a basin, about 31 km, found by Aldersons *et al.* (2003) is confirmed by our study, while large part of the seismicity is related to the basin and thus concentrated in the upper crust down to 20 km depth.

The EBF of the DSB is active over the entire study area except for a small gap related to the transverse BOF. South of the BOF the entire seismicity occurs at the EBF. In this area we found a cluster (red box in Fig. 4) in time and space whose spatial distribution is perpendicular to the main direction of the movement on the main transform fault. This vertical extension of the cluster is probably related to the locking of the region north of it, a nearly aseismic area (Figs 4a and b). The events in the south reflect the ongoing movement of the Arabian Plate to the north. However, the WF show no seismicity in the south during the time of the investigation. North of the BOF similar seismic activity occurs at both boundaries. These earthquakes represent probably the expected transfer of the motion in pull-apart basins from the eastern to the western boundary.

Furthermore the distribution of the seismicity indicate a basin with a vertical EBF going down to a depth of at least 17 km and a 60° eastward dipping western boundary (representing the western boundary fault and the western strike-slip fault), but only traceable down to a depth of 12 km (B and A in Fig. 4c). Our results thus reveal an asymmetric basin. Similar asymmetries have been observed in many other sedimentary basins in strike-slip regimes (e.g. Shedlock *et al.* 1990; Lodolo *et al.* 2003; Uzel & Sözbilir 2008) and also in other basins along the DST (Ben-Avraham 1992). In these cases the basins are bounded by a linear transform segment on the steep side (here the EBF) and normal faults on the other side (here the WF). Thus, asymmetric basins require simultaneous strike-slip motion and transform-normal extension (Ben-Avraham & Zoback 1992).

ACKNOWLEDGMENTS

The work presented here was supported by the Deutsche Forschungsgemeinschaft (DFG) and the Deutsches GeoForschungsZentrum Potsdam (GFZ). We are grateful to Jacek Stankewicz for proofreading the manuscript. All the figures were created with the GMT software (Wessel & Smith 1998). The field installation was done by many people. We are especially grateful to Benjamin Heit and Ayman Mohsen. We thank the GII, the Natural Resources Authority (NRA) of Jordan and the An-Najah National University in Nablus, Palestine, for their support during the field work. The instruments for the field work were provided by the Geophysical Instrument Pool Potsdam (GIPP) of the GFZ. Manual event detection was mainly done by Oliver Rach.

REFERENCES

Aldersons, F., Ben-Avraham, Z., Hofstetter, A., Kissling, E. & Al Yazjeen, T., 2003. Lower-crustal strength under the Dead Sea basin from local earthquake data and rheological modeling, *Earth planet. Sci. Lett.,* **214,** 129–142.

Begin, Z.B. & Steinitz, G., 2005. Temporal and spatial variations of microearthquake activity along the Dead Sea Fault, 1984-2004, *Israel J. Earth Sci.,* **54,** 1–14.

Ben-Avraham, Z., 1992. Development of asymmetric basins along continental transform faults, *Tectonophysics,* **215,** 209–220.

Ben-Avraham, Z. & Lazar, M., 2006. The structure and development of the Dead Sea basin: recent studies, *Geol. Soc. Am.,* **401,** 1–13.

Ben-Avraham, Z. & Ten Brink, U., 1989. Transverse faults and segmentation of basins within the Dead Sea Rift, *J. Afr. Earth Sci.,* **8,** 603–616.

Ben-Avraham, Z. & Zoback, M.D., 1992. Transform-normal extension and asymmetric basins: an alternative to pull-apart models, *Geology,* **20,** 423–426.

ten Brink, U.S., Ben-Avraham, Z., Bell, R.E., Hassouneh, M., Coleman, D.F., Andreasen, G., Tibor, G. & Coakley, B., 1993. Structure of the Dead Sea pull-apart basin from gravity analyses, *J. geophys. Res.,* **98**(B12), 21 877–21 894.

ten Brink, U.S., Al Zoubi, A.S., Flores, C.H., Rotstein, Y., Qabbani, I., Harder, S.H. & Keller, G.R., 2006. Seismic imaging of deep low-velocity zone beneath the Dead Sea basin and transform fault: implications for strain localization and crustal rigidity, *Geophys. Res. Lett.,* **33,** doi: 10.1029/2006GL027890.

Chen, W.-P. & Molnar, P., 1983. Focal depths of intracontinental and intraplate earthquakes and their implications for the thermal and mechanical properties of the lithosphere, *J. geophys. Res.,* **88,** 4183–4214.

van Eck, T. & Hofstetter, A., 1989. Microearthquake activity in the Dead Sea region, *Geophys. J. Int.,* **99,** 605–620.

van Eck, T. & Hofstetter, A., 1990. Fault geometry and spatial clustering of microearthquakes along the Dead Sea–Jordan rift fault zone, *Tectonophysics,* **180,** 15–27.

Freund, R., Garfunkel, Z., Zak, I., Goldberg, M., Weissbrod, T. & Derin, B., 1970. The shear along the Dead Sea rift, *Phil. Trans. R. Soc. Lond.,* **267,** 107–130.

Garfunkel, Z., 1997. The history and formation of the Dead Sea basin, in *The Dead Sea: the Lake and its Setting,* Oxford Monographs on Geology and Geophysics, Vol. 36, pp. 36–56, eds Niemi, T.M., Ben-Avraham, Z. & Gat, J.R., Oxford University Press, Oxford.

Garfunkel, Z. & Ben-Avraham, Z., 1996. The structure of the Dead Sea basin, *Tectonophysics,* **266,** 155–176.

Ginzburg, A. & Ben-Avraham, Z., 1997. A seismic refraction study of the north basin of the Dead Sea, Israel, *Geophys. Res. Lett.,* **24,** 2063–2066.

Husen, S., Kissling, E., Flueh, E. & Asch, G., 1999. Accurate hypocentre determination in the seismogenic zone of the subducting Nazca Plate in northern Chile using a combined on-/offshore network, *Geophys. J. Int.,* **138,** 687–701.

Kissling, E., Ellworth, W.L., Eberhardt-Phillips, D. & Kradolfer, U., 1994. Initial reference models in local earthquake tomography, *J. geophys. Res.,* **99,** 19 352–19 646.

Kissling, E., Kradolfer, U. & Maurer, H., 1995. VELEST user's guide: short introduction, Tech. Rep., ETH Zürich.

Lange, D., 2008. The South Chilean Subduction Zone between 41°–43.5° S: seismicity, structure and state of stress, *Ph.D. thesis*, Universität Potsdam, Potsdam, Germany.

Larsen, B.D., Ben-Avraham, Z. & Shulman, H., 2002. Fault and salt tectonics in the southern Dead Sea basin, *Tectonophysics,* **346,** 71–90.

Lodolo, E., Menichetti, M., Bartole, R., Ben-Avraham, Z., Tassone, A. & Lippai, H., 2003. Magallanes-Fagnano continental transform fault (Tierra del Fuego, southernmost South America), *Tectonics,* **22**(6), doi:10.1029/2003TC001500.

Mechie, J., Abu-Ayyash, K., Ben-Avraham, Z., El-Kelani, R., Qabbani, I., Weber, M. & DESIRE Group, 2009. Crustal structure of the southern Dead Sea basin derived from project DESIRE wide angle seismic data, *Geophys. J. Int.,* **178,** doi:10.1111/j.1365-246X.2009.04161.x.

Meissner, R. & Strehlau, L., 1982. Limits of stresses in continental crusts and their relation to the depth-frequency distribution of shallow earthquakes, *Tectonics,* **1,** 73–89.

Paschke, M., Stiller, M., Ryberg, T., Weber, M. & DESIRE Group, 2011. The shallow *P*-velocity structure of the southern Dead Sea basin derived from near-vertical incidence reflection seismic data in project DESIRE, *Geophys. J. Int.,* **188**, 524–534, doi:10.1111/j.1365-246X.2011.05270.x.

Quennel, A.M., 1958. The structural and geomorphic evolution of the Dead Sea rift, *Q. J. Geol. Soc. London,* **114,** 2–24.

Rydelek, P.A. & Sacks, I.S., 1989. Testing the completeness of earthquake catalogues and the hypothesis of self-similarity, *Nature,* **337,** 251–253.

Shamir, G., 2006. The active structure of the Dead Sea Depression, *Geol. Soc. Am.,* Special Paper **401**, 15–32.

Shedlock, K.M., Brocher, T.M. & Harding, S.T., 1990. Shallow structure and deformation along the San Andreas Fault in Cholame Valley, California, based on high-resolution reflection profiling, *J. geophys. Res.,* **95**(B4), 5003–5020.

Smit, J., Brun, J.-P., Fort, X., Cloetingh, S. & Ben-Avraham, Z., 2008. Salt tectonics in pull-apart basins with application to the Dead Sea Basin, *Tectonophysics,* **449,** 1–16.

Solov'yev, S.L., 1965. Seismicity of Sakhalin, *Bull. Earthq. Res. Inst. Tokyo Univ.,* **43,** 95–102.

Thurber, C., Zhang, H., Waldhauser, F., Hardebeck, J., Michael, A. & Eberhart-Phillips, D., 2006. Three-dimensional compressional wavespeed model, earthquake relocations, and focal mechanisms for the Parkfield, California, Region, *Bull. seism. Soc. Am.,* **96**, 538–549.

Uzel, B. & Sözbilir, H., 2008. A first record of a strike-slip basin in Western Anatolia and its tectonic implication: the Cumaovasi Basin, *Turk. J. Earth Sci.,* **17,** 559–591.

Wesnousky, S.G., 1990. Seismicity as a function of cumulative geologic offset: some observations from southern California, *Bull. seism. Soc. Am.,* **80,** 1374–1381.

Wessel, P. & Smith, W., 1998. New, improved version of the Generic Mapping Tools released, *EOS, Trans., Am. geophys. Un.,* Suppl., **79,** 579.

Zak, I. & Freund, R., 1981. Asymmetry and basin migration in the Dead Sea Rift, *Tectonophysics,* **80,** 27–38.